Journal of Solid State Chemistry 184 (2011) 3310–3318

Contents lists available at SciVerse ScienceDirect

Journal of Solid State Chemistry

journal homepage: www.elsevier.com/locate/jssc

Effect of doping, microstructure, and CO_2 on $La_2NiO_{4+\delta}$-based oxygen-transporting materials

Tobias Klande [a,*], Konstantin Efimov [a], Salvatore Cusenza [b], Klaus-Dieter Becker [b], Armin Feldhoff [a]

[a] Institute of Physical Chemistry and Electrochemistry, Leibniz Universität Hannover, Callinstr. 3-3a, D-30179 Hannover, Germany
[b] Institute of Physical and Theoretical Chemistry, Technische Universität Braunschweig, Hans-Sommer-Str. 10, D-38106 Braunschweig, Germany

ARTICLE INFO

Article history:
Received 22 July 2011
Received in revised form
8 October 2011
Accepted 10 October 2011
Available online 17 October 2011

Keywords:
Mixed ionic-electronic conductor
K_2NiF_4 structure
Carbon dioxide
Long-term stability
Mössbauer
Transmission electron microscopy

ABSTRACT

Alkaline earth-free $La_2NiO_{4+\delta}$ based materials were synthesized by a sol–gel method and studied by X-ray diffraction (XRD), scanning electron microscopy (SEM) and transmission electron microscopy (TEM) techniques as well as oxygen permeation experiments. Effects of doping the nickel position with a variety of cations (Al, Co, Cu, Fe, Mg, Ta, and Zr) were investigated with regards to oxygen flux and microstructure. Doping was always found to diminish the oxygen flux as compared to the reference composition. However, larger grains, which were achieved by longer annealing times at 1723 K have a minor negative impact on oxygen permeation flux in case of $La_2NiO_{4+\delta}$ and $La_2Ni_{0.9}Fe_{0.1}O_{4+\delta}$ system. Mössbauer spectroscopy shows that the iron-doped system exhibits a secondary phase, which was identified by high-resolution transmission electron microscopy (HRTEM) as a higher Ruddlesden-Popper phase. *In-situ* XRD in an atmosphere containing 50 vol% CO_2 and long-term oxygen permeation experiments using pure CO_2 as the sweep gas revealed a high tolerance of the materials towards CO_2.

1. Introduction

Mixed ionic-electronic conductors (MIECs) have received considerable interest over the last few years because of their applicability as oxygen-transporting membranes (OTMs). They can be used in a wide range of applications such as the production of high-purity oxygen [1], in petrochemical processes such as the oxidative coupling of methane to ethylene or ethane (OCM) [2], the partial oxidation of methane to syngas (POM) [3], or as cathode materials in solid-oxide fuel cells (SOFCs) [4]. Also, possible application of OTMs in power plants with CO_2 capture were discussed [5]. Good MIECs contain alkaline-earth metals, e.g., $(La_xSr_{1-x})(Co_yFe_{1-y})O_{3-\delta}$ (LSCF) and $(Ba_xSr_{1-x})(Co_yFe_{1-y})O_{3-\delta}$ (BSCF), which exhibit high oxygen permeabilities because of their high concentrations of oxygen vacancies [6,7]. However, they suffer from instability against CO_2 by forming thermodynamically stable carbonates that act as a barrier for oxygen permeation [8,9]. From thermodynamical calculations via an Ellingham diagram, shown in Fig. 1, it can be expected that $La_2NiO_{4+\delta}$ is stable in CO_2 containing atmospheres at elevated temperatures. However, at temperatures below 1073 K and 1 atm CO_2 the expected decomposition into lanthanum carbonate and nickel oxide may be slow due to kinetic reasons. Recently, Eichhorn Colombo et al. showed long-term CO_2 stability of La_2NiO_4 using permeation experiments in CO_2 at different temperatures [14]. In the present article the CO_2 stability was further investigated by *in-situ* XRD and long-term permeation experiments under CO_2 containing atmospheres. Another hindrance is the relative high coefficient of linear thermal expansion (CTE) of 3D conducting perovskites, typically between 20×10^{-6} and $24\times10^{-6}\,K^{-1}$ [15,16]. Compared to the CTEs of standard electrolytes such as yttrium-stabilized zirconia (YSZ) or gadolinium-doped ceria (CGO), which exhibit CTE values of approximately $10\times10^{-6}\,K^{-1}$, this poor thermomechanical compatibility may lead to mechanical stress and cracking during operational processes. With relatively low CTE values between $11.9\times10^{-6}\,K^{-1}$ and $13.8\times10^{-6}\,K^{-1}$ $La_2NiO_{4+\delta}$ seems to be suitable for applications in integrated systems [17,18]. The Ruddlesden–Popper-phase perovskite-related $La_2NiO_{4+\delta}$ is a prominent candidate for ceramic membranes with long-term stability. The crystal structure, as shown in Fig. 2, is built from alternating perovskite-like and rock-salt-like layers arranged along the *c*-axis. The oxygen transport through $La_2NiO_{4+\delta}$ occurs at elevated temperatures mainly via a 2D interstitial migration mechanism in the rock-salt-like layers [19] but also to a small extent via oxygen-vacancy migration through the perovskite-like layers. Several groups observed ordering of bound interstitial excess oxygen in superstructures at 9 and 300 K by transmission electron microscopy (TEM) [20,21]. Furthermore, Skinner et al. reported phase transitions in this system that were detected with *in-situ* high-temperature neutron powder diffraction. The transitions occur between the orthorhombic and tetragonal modifications at low temperatures ($T<423$ K) [22]. The tetragonal structure is then maintained over a temperature range of 423–1073 K on heating and cooling, and loss of

* Corresponding author.
E-mail address: tobias.klande@pci.uni-hannover.de (T. Klande).

0022-4596/$ - see front matter © 2011 Elsevier Inc. All rights reserved.
doi:10.1016/j.jssc.2011.10.019

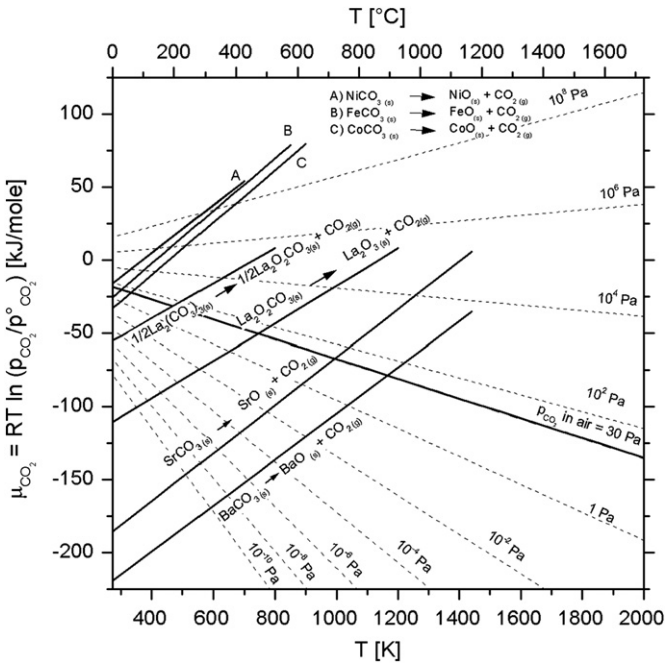

Fig. 1. Ellingham diagram with decomposition temperatures of carbonates under different CO_2 partial pressures. Chemical potential of CO_2 above $NiCO_3$, $FeCO_3$, $CoCO_3$, $La_2O_2CO_3$, $SrCO_3$, and $BaCO_3$ were calculated from thermodynamic data [10–12]. The chemical potential of $La_2(CO_3)_3$ was determined experimentally [13]. The dashed lines represent the chemical potential of CO_2 in the surrounding atmosphere for different partial pressures. $p^\circ(CO_2) = 101.3$ kPa refers to standard conditions.

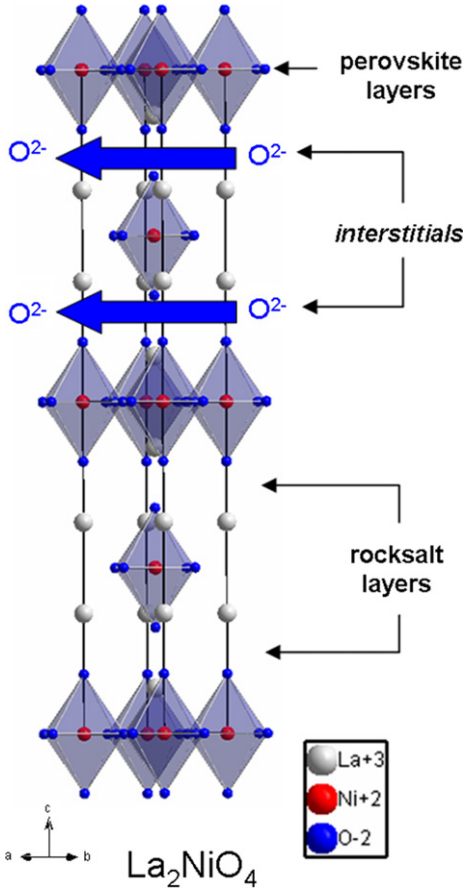

Fig. 2. $La_2NiO_{4+\delta}$ shown with arrangement of bulding blocks along the c-axis; the arrows indicate the diffusion of interstitial oxygen through the rock-salt layers (structure data ICSD no. 1179).

interstitial oxygen was detected up to a temperature of 723 K. These phase transitions do not influence oxygen-permeation properties in the intermediate temperature range ($T = 773$–1073 K) and the behavior at these temperatures has yet to be investigated by *in-situ* TEM. $La_2NiO_{4+\delta}$ offers the above mentioned advantages, but the oxygen flux is poor compared to perovskite materials such as BSCF. The present work is focused on a systematical overview of the influence of different dopants on the oxygen-permeation fluxes in the $La_2NiO_{4+\delta}$ system. In the stoichiometric base compound, the A-site cation lanthanum is trivalent and the B-site cation nickel is divalent. Due to oxygen hyperstoichiometry a significant amount of nickel is oxidised to the trivalent state. By doping of the B-site with different cations of increasing valence the interstitial oxygen content can be influenced. By changing the concentration of interstitials, which are the main diffusing species [19], an effect can be assumed on oxygen permeation, which may result in oxygen transport membranes with enhanced properties. Furthermore, in this article the influence of grain size on oxygen flux was investigated for $La_2NiO_{4+\delta}$ and $La_2Ni_{0.9}Fe_{0.1}O_{4+\delta}$. Previously, various groups reported an influence of grain size on the functional characteristics of several MIEC materials [23–26]. By optimizing the microstructure of the perovskite related $La_2NiO_{4+\delta}$ materials properties can be improved. The results of TEM studies and Mössbauer experiments on the iron-doped $La_2NiO_{4+\delta}$ are also reported.

2. Experimental

2.1. Sample preparation

The powders were synthesized by the sol–gel route using stoichiometric amounts of metal oxides, ethylenediaminetetraacetic acid (EDTA) and citrate, as described elsewhere [27–29]. After the reactants were fired in a heating mantle, the obtained products were pre-calcined at 1173 K with a heating and cooling rate of 3 K min^{-1}. The powders were uniaxially pressed into 16 mm green bodies at 50 kN for 15 min. Gas-tight membranes for oxygen-permeation measurements with a thickness of 1 mm were then sintered in air at 1723 K with an annealing time of 10, 40 or 140 h with a heating and cooling rate of 2 K min^{-1}. Samples for Mössbauer experiments, enriched with ^{57}Fe, were prepared under the same conditions with an annealing time of 10 h at 1723 K. An overview of all doped materials is shown in Table 1.

2.2. X-ray diffraction analysis

X-Ray diffraction (XRD) analysis was performed at room temperature using a Bruker-AXS D8 Advance diffractometer equipped with a

Table 1
Overview of the base material $La_2NiO_{4+\delta}$ and doped $La_2Ni_{0.9}M_{0.1}O_{4+\delta}$ solid solutions: unit cell parameters from XRD, estimated effective grain diameter from scanning electron microscope surface-views, activation energy of oxygen permeation in the temperature range from 1023 to 1123 K, and secondary phases obtained by XRD except for the iron-doped sample (marked by *) by high-resolution transmission electron microscopy and Mössbauer spectroscopy.

Composition	Unit cell parameters		Grain diameter	Activation energy	Secondary phase
	a (nm)	c (nm)	(μm)	(kJ mol^{-1})	
$La_2NiO_{4+\delta}$	0.3862	1.2683	1.8	56.7	–
$La_2Ni_{0.9}Zr_{0.1}O_{4+\delta}$	0.3863	1.2698	0.4	67.0	$La_2Zr_2O_7$
$La_2Ni_{0.9}Al_{0.1}O_{4+\delta}$	0.3862	1.2689	0.8	75.9	$La_3Ni_2O_7$
$La_2Ni_{0.9}Fe_{0.1}O_{4+\delta}$	0.3876	1.2671	1.2	75.3	$La_4Ni_{2.1}Fe_{0.9}O_{10}$*
$La_2Ni_{0.9}Co_{0.1}O_{4+\delta}$	0.3867	1.2649	2.7	54.1	–
$La_2Ni_{0.9}Mg_{0.1}O_{4+\delta}$	0.3864	1.2687	3.3	58.4	La_2O_3
$La_2Ni_{0.9}Cu_{0.1}O_{4+\delta}$	0.3858	1.2729	5.3	66.9	$La_3Ni_2O_7$

Cu $K\alpha$ radiation source. Data sets were recorded in step-scan mode in the angular range of $20^\circ \leq 2\theta \leq 60^\circ$ at an interval of 0.02°. High-temperature measurements were conducted in an *in-situ* cell (HTK-1200 N, Anton Paar) between room temperature and 1273 K under an atmosphere of 50 vol% CO_2/50 vol% air. The heating rate was 12 K min^{-1} with an equilibration time of 30 min before each measurement.

2.3. Mössbauer spectroscopy

Transmission Mössbauer spectroscopy (TMS) was performed on $La_2Ni_{0.9}Fe_{0.1}O_4$ powder, which was obtained by grinding dense ceramics. The powder was synthesized by using a metallic iron precursor, which was 96.63% enriched in ^{57}Fe (Chemotrade) and were used without any further treatment. A standard Halder Mössbauer system was employed in constant acceleration mode with a ^{57}Co/Rh γ-ray source. The spectra were fitted by employing the general Mössbauer spectral analysis software *Recoil* [30] using lineshape functions accounting for a distribution of quadrupolar interactions. The velocity calibration was performed using α-Fe foil, and the isomer shifts are stated relative to the center of this calibration.

2.4. Scanning electron microscopy

Field-emission scanning electron microscopy (FE-SEM) imaging was performed using a JEOL JSM-6700 F field-emission instrument at a low excitation voltage of 2 kV. For backscattered-electron channeling contrast imaging at higher excitation voltages, samples were polished to crystallinity by vibration polishing and then investigated using a JEOL JSM-6510 QSEM.

2.5. Transmission electron microscopy

TEM investigations were performed at an accelerating voltage of 200 kV on a JEOL JEM-2100 F-UHR field-emission instrument (C_S=0.5 mm, C_C=1.2 mm). The microscope was operated as a high-resolution TEM (HRTEM) as well as a scanning TEM (STEM) in high-angle angular dark field (HAADF) mode. The preparation method of the TEM specimen is described in detail elsewhere [8]. HRTEM multislice simulations were performed using JEMS software.

2.6. Oxygen permeation measurements

Oxygen permeation was measured in a custom-made high-temperature permeation cell, as described elsewhere [23,31]. The membranes were sealed on an alumina tube with a gold cermet (Heraeus). The feed side was fed with synthetic air (20 vol% O_2/80 vol% N_2) at a rate of 150 mL min^{-1}, whereas Ne (1.0 mL min^{-1}, 99.995%) and He (29.0 mL min^{-1}, 99.995%) or CO_2 (29.0 mL min^{-1}, 99.995%) were fed to the sweep side. An Agilent 7890 gas chromatograph with a Carboxen 1000 column was employed to analyze the gas mixture. The absolute flux rate was calculated using neon as an internal standard. The total O_2 leakage was calculated and subtracted from the total O_2 flux after the N_2 concentration was measured.

3. Results and discussion

3.1. X-ray diffraction

The XRD patterns of the different materials (Fig. 3) showed the formation of $La_2NiO_{4-\delta}$-type phases, which can be indexed as the tetragonal K_2NiF_4 (S.G. *I*4/*mmm*) structure (ICSD no. 1179), which is typical for $La_2NiO_{4+\delta}$ at high temperatures and air atmosphere. This structure is metastable at room temperature and can accommodate

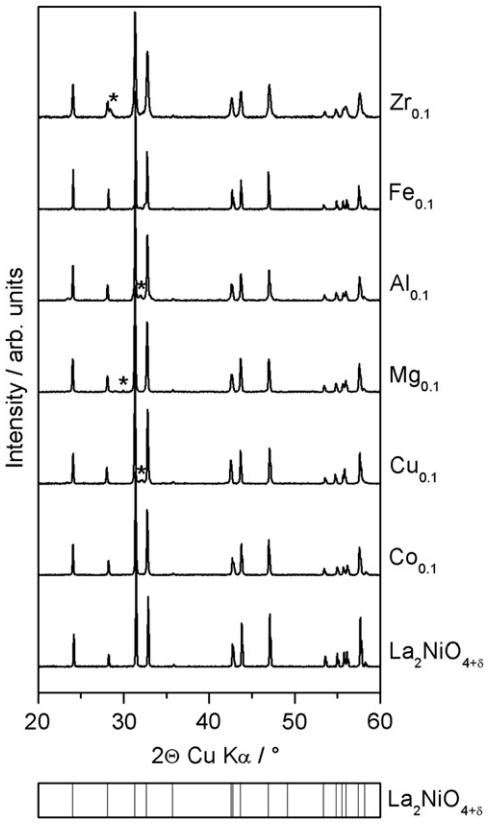

Fig. 3. Room-temperature XRD patterns of $La_2NiO_{4+\delta}$ membranes with different dopants on the Ni site. The theoretical Bragg positions for $La_2NiO_{4+\delta}$ (ICSD 1179) are labeled at the bottom of the figure.

various oxygen hyperstoichiometries. No other main crystalline phases were observed. However, some powders exhibited a low amount of additional reflections, which are marked by asterisks. In the Zr-doped system, the additional reflection at 28.3° can be attributed to the (2 2 2) reflection of $La_2Zr_2O_7$ (ICSD no.154752). The Al- and Cu-doped systems exhibit additional reflections at 31.9°, which can be assigned to the (1 0 5) reflection of Ruddlesden–Popper type by-phase $La_3Ni_2O_7$ (ICSD no. 155320). In the Mg-doped system, the reflection at 29.9° corresponds to the (0 1 1) reflection of La_2O_3 (ICSD no. 56166). No pure phase could be obtained by tantalum doping. With respect to the sensitivity of XRD, no other crystalline phases were found. By doping the B-site with cations of different valence oxygen hyperstoichiometry should be affected. The general trend for $La_2NiO_{4+\delta}$ observed by Rice and Buttrey [32] is for unit cell parameter *a* to decrease and *c* to increase with increasing δ. Furthermore, it can be expected that cell parameters change by doping according to the dopant's ionic radius. However, no trend can be derived from variation in lattice parameters for the Al-, Cu-, Mg- and Zr-doped systems (see table 1). The change is within the limits of experimental error. The unit cell parameters for the base system as well as for the cobalt- and iron-doped systems are in good agreement with the literature [33–35]. Because CO_2 stability is an important factor for membrane applicability, *in-situ* XRD measurements were performed on the undoped $La_2NiO_{4+\delta}$ system in the temperature range of 303–1273 K in an atmosphere containing 50 vol% CO_2 and 50 vol% air. Fig. 4 shows no additional reflections that would indicate the presence of other phases, e.g., carbonates or phase transitions during heating or cooling. Using the temperature-dependent shift of the cell volume during these measurements, the CTE was estimated to be 15.1×10^{-6} K^{-1} in an atmosphere containing 50 vol% CO_2 and 50 vol% air. This result agrees with the values reported in the literature of 11.9×10^{-6} K^{-1} and 13.8×10^{-6} K^{-1}

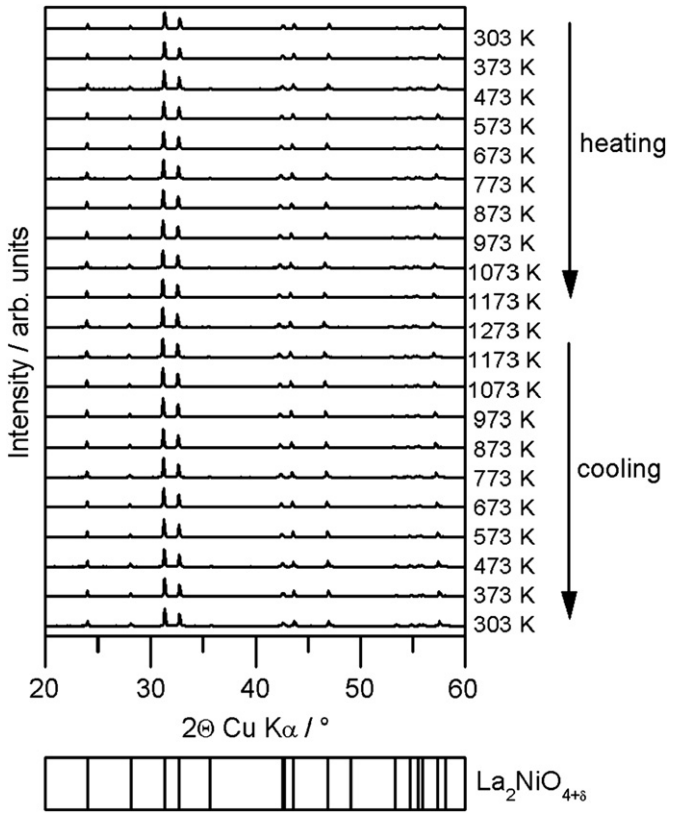

Fig. 4. *In-situ* XRD patterns of $La_2NiO_{4+\delta}$ under 50 vol% CO_2 and 50 vol% air; heating and cooling rate: 12 K min^{-1}, equilibration time at each temperature: 30 min.

measured in air [17,18]. Compared to 3D perovskites, which exhibit values between $20\times10^{-6}\,K^{-1}$ and $24\times10^{-6}\,K^{-1}$ [15,16,36,37], $La_2NiO_{4+\delta}$ possesses a better thermomechanical compatibility, which assures stability in integrated systems such as membrane reactors or SOFCs.

3.2. Membrane microstructure

The microstructures of all membranes were examined using FE-SEM. No cracks or pores were visible on the surfaces of the membranes. In the bulk material only a few non-connected pores were observed. The average grain size was analyzed using the Image J [38] particle analyzer by measuring the grain area in μm^2 and then the effective grain diameter was estimated by assuming circle-shaped grains. Table 1 shows the average grain size for the base material and $La_2Ni_{0.9}M_{0.1}O_{4+\delta}$ (M= Al, Co, Cu, Fe, Mg, Zr). Although the amount of doping is as low as 10 mol%, significant differences in the average grain-size area were observed which increased in the order $Zr^{4+} < Al^{3+} < Fe^{3+} < Ni^{+2} < Co^{+2} < Mg^{+2} < Cu^{+2}$. The copper-doped $La_2NiO_{4+\delta}$ solid solution exhibited the largest grains, with an average size of 5.3 μm, whereas mixed crystals with the highly charged zirconium provided the smallest grains at 0.4 μm. From our data, a general trend can be discerned. Cations with low oxidation states favor the formation of large grains, whereas more highly charged ions favor the formation of small grains. Grain size can therefore be directly controlled by doping with metal cations possessing different valences, which results in tailor-made solid solutions. This doping may affect the oxygen-permeation properties with respect to grain or grain-boundary diffusion and surface exchange reactions. However, it is difficult to differentiate between grain size and doping effects and to correlate this to functional properties such as chemical stability and, especially, oxygen flux.

3.3. Oxygen permeation

Oxygen-permeation measurements were conducted in the temperature range of 1023–1223 K. Fig. 5 shows the oxygen-permeation flux of the base material and $La_2Ni_{0.9}M_{0.1}O_{4+\delta}$ (M= Al, Co, Cu, Fe, Mg, Ni, Zr) from air (feed side) to helium (sweep side) at different temperatures. The doping of the Ni site affects the oxygen-permeation performance of the membranes. The highest flux rate of 0.47 mL min^{-1} cm^{-2} at 1223 K was achieved on a 1 mm thick undoped $La_2NiO_{4+\delta}$ membrane. The iron-doped membrane $La_2Ni_{0.9}Fe_{0.1}O_{4+\delta}$ exhibited a flux rate of 0.46 mL min^{-1} cm^{-2} at 1223 K, which is similar to that of the undoped system. However, doping was found to always diminish the oxygen-permeation rate at 1223 K, which decreases in the order $Fe^{3+} > Co^{2+} > Zr^{4+} \approx Mg^{+2} \approx Al^{3+} \approx Cu^{+2}$. No dependence of the permeation rate on the doped ion's regular valence was observed. The regular oxidation state of Ni cations in the $La_2NiO_{4+\delta}$ structure is divalent, and a partial amount of the Ni is oxidised to the trivalent state to compensate for the incorporation of excess oxygen. From this point of view, it would be favorable to insert higher-valence cations to increase the oxygen-carrier concentrations and, therefore, the oxygen-permeation performance. However, no significant improvement was observed in this respect. It can be expected that the interstitial oxygen content increases by doping with Al^{3+}, Fe^{3+}, and Zr^{4+} and decreases by doping with Cu^{2+} ,Mg^{2+} and Co^{2+}. However, recently, Kharton et al. reported the results of static lattice and molecular dynamics calculations [39] on the $La_2NiO_{4+\delta}$ system and the incorporation of iron, copper and cobalt. These computations showed that the incorporation of higher-valence ions increases the ionic charge-carrier concentration, but the mobility of the oxygen anions in both layers of the $La_2NiO_{4+\delta}$ structure is reduced. We observed, in general, that the doping of the Ni site leads to a reduction of the oxygen-permeation performance. However, as proposed by Kharton et al. [35] two contributions to the total ionic conductivity play a decisive role: ionic conduction in the perovskite layers due to oxygen vacancy migration and the interstitial oxygen mechanism. By doping on the B-site both mechanisms may be affected in a positive or negative way. This may explain our above described experimental results and is consistent with literature data on $La_2Ni_{0.9}Co_{0.1}O_{4+\delta}$ [34] and $La_2Ni_{0.9}Fe_{0.1}O_{4+\delta}$ [35] membrane materials, which exhibit a smaller flux than undoped $La_2NiO_{4+\delta}$ [40]. A correlation of the grain sizes, which were reported in Section 3.2, with the oxygen-permeation rates is difficult. Apparently, larger grains, as observed in the copper- and

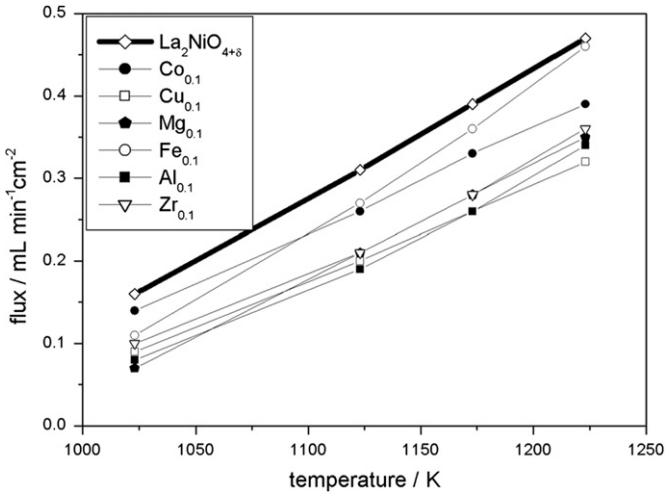

Fig. 5. Oxygen permeation rate of the base material, $La_2NiO_{4+\delta}$, and $La_2Ni_{0.9}M_{0.1}O_{4+\delta}$ (M= Al, Co, Cu, Fe, Mg, Zr); membrane thickness: 1 mm, feed side: 150 mL min^{-1} synthetic air, sweep side: 29 mL min^{-1} He and 1 mL min^{-1} Ne.

magnesium-doped $La_2NiO_{4+\delta}$, exhibit low oxygen fluxes. In contrast to this observation, the zirconium- and aluminum-doped samples, which provide the smallest grains, also show low fluxes. This disagreement shows as well, that for improving the overall permeation flux all parameters have to be carefully considered. The activation energies of oxygen diffusion in the temperature range from 1023 to 1223 K were estimated from the Arrhenius representation; the results are summarized in Table 1. The base and cobalt-doped materials exhibit the lowest activation energies of 56.7 kJ mol^{-1} and 54.1 kJ mol^{-1}, respectively. The activation energy of the iron-doped system, at 75.3 kJ mol^{-1}, is slightly higher. These results are in good agreement with data from the literature, where values of 52.1 kJ mol^{-1} for $La_2NiO_{4+\delta}$ [41] and 69–80 kJ mol^{-1} for $La_2Ni_{0.9}Fe_{0.1}O_{4+\delta}$ [42] were reported. To assess the CO_2 stability during the permeation experiments, a long-term measurement was conducted over 120 h using pure CO_2 as the sweep gas. As is evident in Fig. 6, a constant O_2 permeation flux was observed. Nevertheless, the oxygen-permeation rate is lower than that achieved with pure helium on the sweep side. The decrease of oxygen flux at the start of the measurement may be explained by the inhibiting effect of CO_2 on the surface exchange reaction, which hinders the release of oxygen from the solid surface due to reaction of absorbed CO_2 species with the oxygen vacancies on the membrane surface [43]. Furthermore, the fact that the oxygen surface exchange had various rates in different gas atmospheres is well known and was discussed in detail elsewhere [44–46]. Compared to alkaline-earth-containing materials, e.g., $(La_{0.4}Sr_{0.6})(Co_{0.8}Fe_{0.2})O_{3-\delta}$, which was measured by our group, the oxygen-permeation flux of $La_2NiO_{4+\delta}$ is maintained for more than 100 h, whereas the Sr-containing material exhibits a slow decline in the flux and broke down completely after operating for 60 h. Although $La_2NiO_{4+\delta}$ shows a lower flux than $(La_{0.4}Sr_{0.6})(Co_{0.8}Fe_{0.2})O_{3-\delta}$, it possesses excellent long-term stability in nearly 100 vol% CO_2 sweep gas at 1173 K.

3.4. Influence of membrane microstructure on oxygen permeation

It was reported that grain or grain boundary interactions play a key role in ionic conduction [23–26]. Many perovskite materials show an increase in oxygen conductivity by increasing the grain size. For perovskite related La_2NiO_4 based materials this was not yet investigated. To investigate the influence of the grain size and grain boundaries in detail, two samples were chosen. To change the grain size, annealing times of 10, 40 and 140 h at 1723 K were applied to

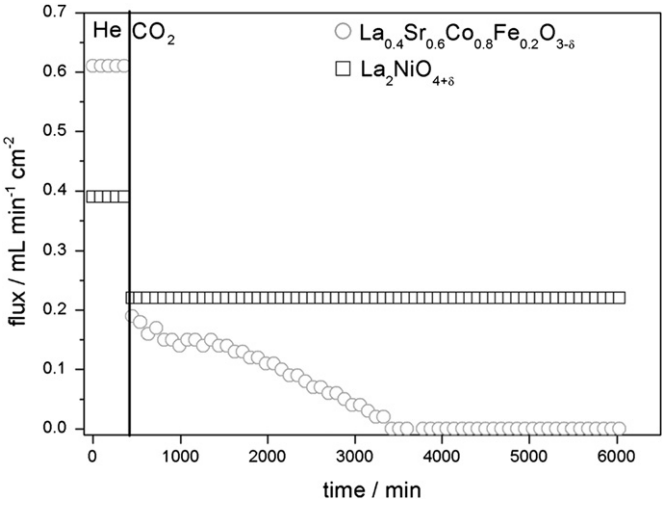

Fig. 6. Oxygen flux rate of $La_2NiO_{4+\delta}$ and $(La_{0.4}Sr_{0.6})(Co_{0.8}Fe_{0.2})O_{3-\delta}$ membranes at 1173 K with a thickness of 1 mm, feed side: 150 mL min^{-1} synthetic air, sweep side: 29 mL min^{-1} He or CO_2 and 1 mL min^{-1} Ne.

Table 2
The dependence of the average grain size on annealing time and the estimated effective grain diameters for $La_2NiO_{4+\delta}$ and $La_2Ni_{0.9}Fe_{0.1}O_{4+\delta}$.

Dwell time (h)	10	40	140
Effective grain diameter $La_2NiO_{4+\delta}$ (μm)	1.8	2.7	4.6
Effective grain diameter $La_2Ni_{0.9}Fe_{0.1}O_{4+\delta}$ (μm)	1.2	1.7	8.2

samples of $La_2NiO_{4+\delta}$ and $La_2Ni_{0.9}Fe_{0.1}O_{4+\delta}$. Table 2 shows the average grain sizes that were obtained by this treatment, whereas Fig. 7 a–c shows the SEM images of the surfaces of the $La_2Ni_{0.9}Fe_{0.1}O_{4+\delta}$ membranes that were sintered for different annealing times. In addition, a surface view of a $La_2NiO_{4+\delta}$ membrane that was polished to crystallinity and then examined by the channeling contrast technique is shown in Fig. 7d. As is evident in the figures, grain growth was induced by longer sintering times. The base material exhibits grain sizes of 1.8, 2.7 and 4.6 μm^2 for the membranes sintered for 10, 40 and 140 h, respectively. The oxygen flux decreases from 0.47 to 0.41 to 0.31 mL min^{-1} cm^{-2} with increasing grain size and, therefore, with decreasing amount of grain boundaries. For the iron-doped sample, average grain sizes of 1.2, 1.7 and 8.2 μm^2 were obtained after annealing times of 10, 40 and 140 h. The oxygen flux was 0.46 mL min^{-1} cm^{-2}, which increased slightly to 0.49 mL min^{-1} cm^{-2} and then decreased to 0.39 mL min^{-1} cm^{-2}. Thus, the base material shows lower fluxes with increasing grain size (Fig. 8), whereas for the iron-doped samples, this effect is less pronounced. To conclude, our experimental findings show a negative effect of an increased grain size on oxygen permeation. This may be related to faster grain boundary diffusion, which may be more favorable in case of the predominantly 2D-conducting interstitial mechanism in $La_2NiO_{4+\delta}$.

3.5. Mössbauer measurements on $La_2Ni_{0.9}Fe_{0.1}O_4$

Transmission Mössbauer measurements were performed at 298 K, Fig. 9. As is evident in the figure, the spectra are dominated by a doublet with a quadrupole splitting of about QS(I)=1.4 mm/s. However, due to the slight asymmetry visible at its center, a second doublet with a smaller splitting, QS(II), of about 0.4 mm/s is required for a consistent and appropriate fit of the spectrum. The spectrum was fitted with Voigt model functions which allow for a distribution of quadrupolar interactions at the nuclei. According to Menil et al. [47], the observed isomer shift IS(I) of the doublet with the larger quadrupole splitting, Table 3, can be attributed to octahedrally coordinated Fe^{3+}. The shift IS(II) of the second quadrupole doublet approaches the range expected for Fe^{4+}. Thus, the second doublet may be attributed to an iron species with a mixed Fe^{3+}/Fe^{4+} charge state where the difference in the experimental isomer shifts, IS(I)–IS(II), amounts to about 0.2 mm/s. For comparison, note that in the case of the system (La,Sr)(Fe,Mn)O_3 a value of 0.3 mm/s was obtained for the difference in shifts for Fe^{3+} and Fe^{4+} [48]. Because Fe^{3+} is known to occupy Ni^{2+} regular positions in $La_2Ni_{0.9}Fe_{0.1}O_{4+\delta}$ [49], the spectroscopically detected presence of a second iron species possessing a Fe^{3+}/Fe^{4+} charge state suggests the presence of a secondary phase. In fact, according to the phase diagram for La–Fe–Ni–O reported by Kiselev et al. for 1370 K, the sample under investigation in the present study, $La_2Ni_{0.9}Fe_{0.1}O_{4+\delta}$, should consist of three phases at high temperatures: La_2O_3, $La_2Ni_{0.9}Fe_{0.1}O_{4+\delta}$ and $La_4Ni_{2.1}Fe_{0.9}O_{10-\delta}$ [50]. Here, the latter phase may contain a mixed-valent iron component and, thus may be associated with the experimentally observed secondary phase. This phase composition is also consistent with our TEM observations, see below. In conclusion, our observation of two quadrupole-split subspectra due to iron ions of different valency is compatible

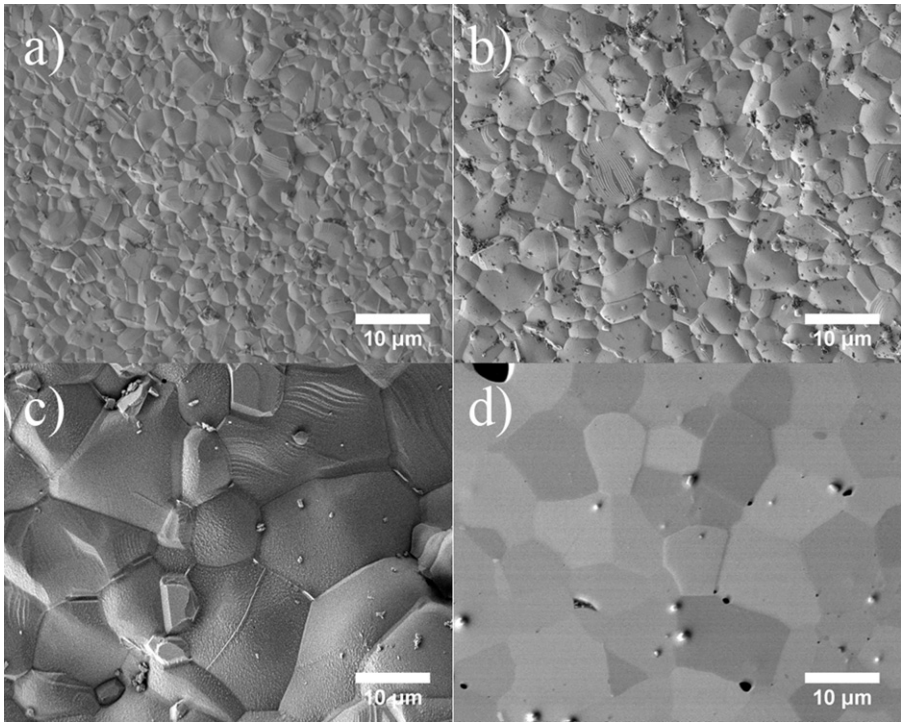

Fig. 7. SE surface view micrographs of the grain structure of $La_2Ni_{0.9}Fe_{0.1}O_{4+\delta}$ with different sintering times (a) 10 h, (b) 40 h and (c) 140 h and (d) $La_2NiO_{4+\delta}$ 140 h channeling contrast image.

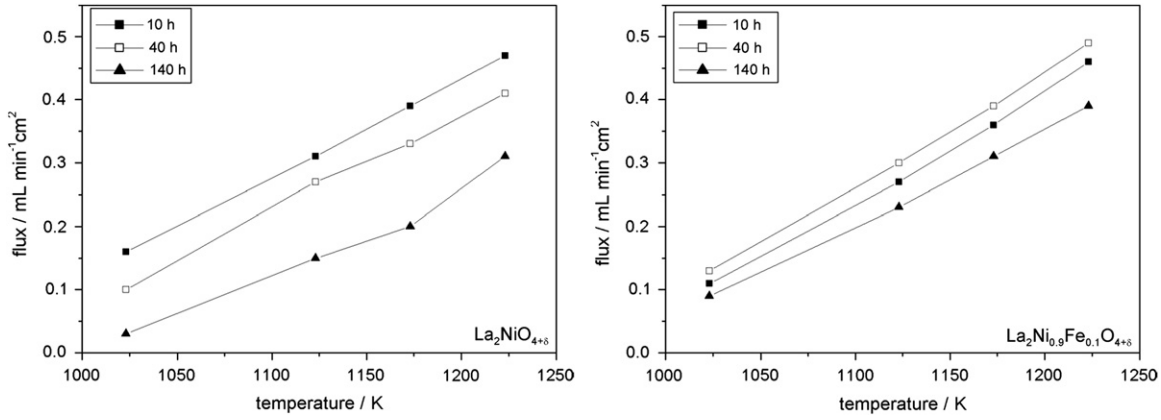

Fig. 8. Oxygen-permeation flux of the base material, $La_2NiO_{4+\delta}$, and $La_2Ni_{0.9}Fe_{0.1}O_{4+\delta}$ after different annealing times.

with the admittedly incomplete information available for the La–Fe–Ni–O phase diagram.

Previously, ^{57}Fe Mössbauer absorption spectra of $La_2Ni_{1-x}Fe_xO_{4+\delta}$ have been reported by Fontcuberta et al. ($x \approx 0.02$) [49] and by Tsipis et al. ($x=0.1$) [51]. However, whereas Tsipis et al. [51] reported a strictly symmetrical signal that could be fitted with a single quadrupole doublet, the spectrum obtained by Fontcuberta et al. [49] is strongly asymmetric and requires three quadrupole doublets for an acceptable fit. Good agreement is observed between the present study and spectral parameters reported in the literature for the dominating doublet possessing the largest splitting, see Table 3. In respect to the secondary contributions in their spectrum which amount up to 30% of total intensity, Fontcuberta et al. [49] speculate that these could be due to iron ions incorporated into intergrowth phases, $La_{2+n}Ni_{1+n}O_{4+3n}$. Indeed, the presence of such a phase, $La_4Ni_3O_{10}$ with $n=2$, is confirmed by the present results obtained by TEM as is reported below. A striking discrepancy, however, remains in respect to the isomer shift of the secondary contribution(s) to the Mössbauer spectra. Whereas the two secondary subspectra observed by Fontcuberta et al. [49] most probably are due to Fe^{3+} ions, the isomer shift observed in the present work indicates a Fe^{3+}/Fe^{4+} mixed-valent charge state of iron. According to Tsipis et al. [52], in bulk $La_4Ni_{2.7}Fe_{0.3}O_{10-\delta}$ iron is present as Fe^{3+} exclusively. A possible reason for this discrepancy with the present work may be due to the fact that the secondary intergrowth phase in our sample is present as lamellae possessing thicknesses of the order of 10 nm, see below, and that the electronic structure of these nanophases is not yet comparable with that of the bulk. Alternatively, the secondary signal observed in our sample could be due to iron ions in the bulk of $La_2Ni_{1-x}Fe_xO_{4+\delta}$ which compensate for the excess of interstitial oxygen. Further work, including an *in-situ* Mössbauer study at high temperatures, is under way to solve these open questions.

3.6. HRTEM and SAED

Samples of $La_2NiO_{4+\delta}$ and $La_2Ni_{0.9}Fe_{0.1}O_{4+\delta}$ were vibrational polished to preserve crystallinity to the very surface and then

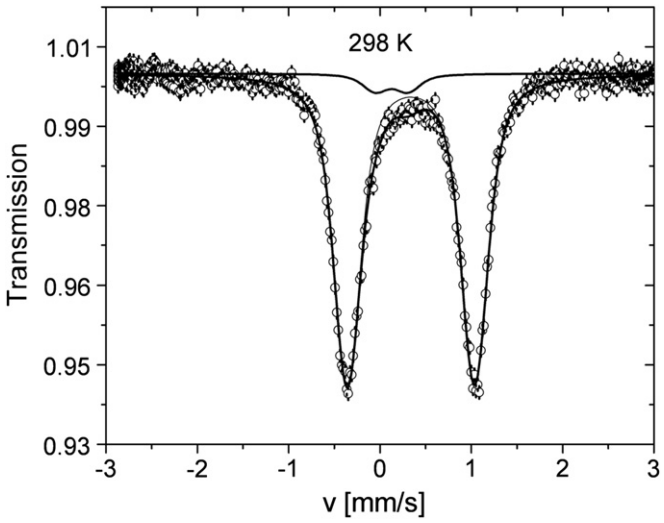

Fig. 9. Mössbauer spectrum of $La_2Ni_{0.9}Fe_{0.1}O_{4+\delta}$ at 298 K.

Table 3
Mössbauer fitting result for $La_2Ni_{0.9}Fe_{0.1}O_{4+\delta}$ at room temperature from present work and from literature: *A* – area fraction (error), $\langle\delta\rangle$ – mean values of isomer shift (vs α-Fe) and $\langle\Delta\rangle$ – mean values of quadrupolar splitting.

temperature (K)	State	A (%)	$\langle\delta\rangle$ (mm/s)	$\langle\Delta\rangle$ (mm/s)	Ref.
298	Fe^{3+}	95.2(14)	0.339(1)	1.409(3)	This work
	Fe^{3+}/Fe^{4+}	4.8(14)	0.13(4)	0.36(6)	
295	Fe^{3+}	68(2)	0.322(1)	1.440(4)	[49]
	Fe^{3+}	19(4)	0.295	0.85(2)	
	Fe^{3+}	13(4)	0.267(6)	0.40(3)	
295	Fe^{3+}	100	0.33	1.35	[51] in air
	Fe^{3+}	100	0.34	1.31	[51] in oxygen

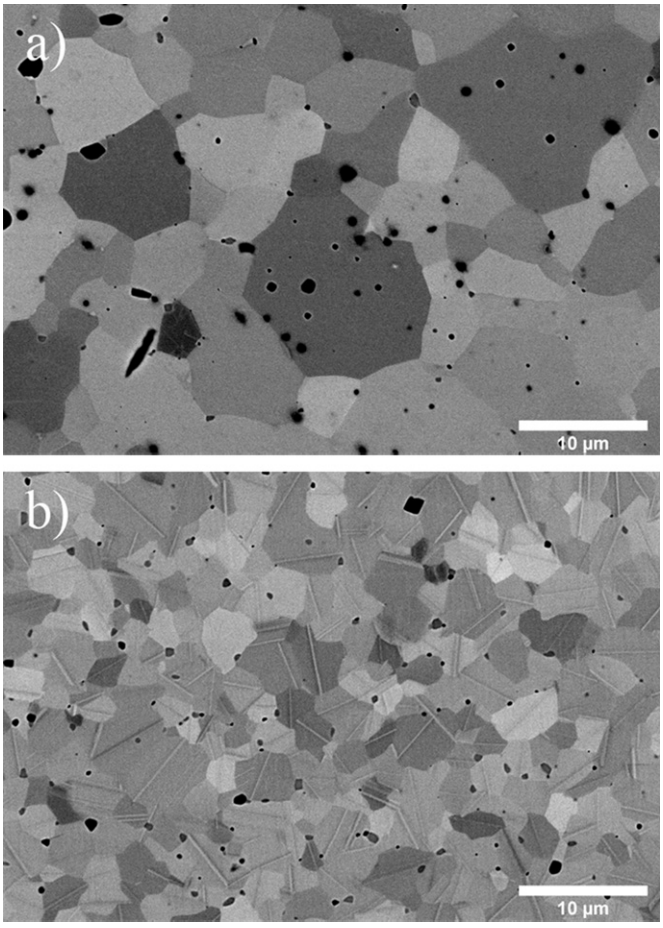

Fig. 10. (a) The polished-surface channeling contrast images of $La_2NiO_{4+\delta}$ sintered for 10 h and (b) $La_2Ni_{0.9}Fe_{0.1}O_{4+\delta}$ sintered for 10 h.

investigated using backscattered-electron channeling contrast imaging. In Fig. 10, $La_2NiO_{4+\delta}$ showed no formation of a foreign phase, whereas $La_2Ni_{0.9}Fe_{0.1}O_{4+\delta}$ showed numerous lamellae-like structures inside the host grains. A different iron-containing phase was detected by our Mössbauer experiment. The grain boundaries were examined in detail to find possible by-phases. Furthermore, the nature of the grain boundaries might be a key factor for the oxygen permeation performance. Three grains are shown in Fig. 11a: the upper grain is oriented along zone axis [3 1 1], the lower is oriented along zone axis [1 1 0] and the grain on the left side of the micrograph is not oriented. No amorphous or other phases were observed at the interface between the two oriented grains, see Fig. 11b. Therefore, the different grains are in intimate contact without contaminations inside the grain boundaries. As stated previously, according to the phase diagram of Kiselev et al. [50], the sample should consist at high temperatures of the three different phases: La_2O_3, $La_2Ni_{0.95}Fe_{0.05}O_{4+\delta}$, and $La_4Ni_{2.1}Fe_{0.9}O_{10-\delta}$. As shown in Section 3.1, $La_2Ni_{1-x}Fe_xO_{4+\delta}$ is indeed the main phase, as confirmed by XRD. With respect to the sensitivity of XRD, the other phases in low concentrations may not be detectable. The perovskite-related Ruddlesden–Popper phase, which is characterized by a different stacking sequence of the successive *c*-axis, was observed as an intergrowth in several $La_2Ni_{1-x}Fe_xO_{4+\delta}$ host grains. As seen in the HAADF-STEM image (Fig. 12 a), the lamella goes through the whole host grain. HRTEM (Fig. 12 b,c) reveals the interface between the $La_2Ni_{1-x}Fe_xO_{4+\delta}$ and $La_{2+n}Ni_{1+n}O_{4+3n-\delta}$ phases. The lamella is approximately 15–30 nm thick. The SAED pattern in Fig. 12d shows $La_2Ni_{1-x}Fe_xO_{4+\delta}$ along the [1 1 0] zone axis. Fig. 12e shows the superposition of the SAED patterns from the host grain and the detected $La_{2+n}Ni_{1+n}O_{4+3n-\delta}$ intergrowth phase. Via EDXS, an enrichment of iron could be detected in the lamella. The simulated HRTEM contrast images for $La_4Ni_3O_4$ and La_2NiO_4 phases (Fig. 12c) via the JEMS software using the multislice method are in good agreement with our experimental data. Therefore, according to the SAED and the JEMS simulation, the intergrowth can be clearly indexed as an iron-containing $La_4Ni_3O_4$ phase which is in accordance with the present Mössbauer and TEM observations. Because La_2O_3 was also detected by EDXS, we conclude that La_2–$Ni_{0.95}Fe_{0.05}O_{4+\delta}$ is the main phase and that $La_4Ni_{2.1}Fe_{0.9}O_{10-\delta}$ and La_2O_3 are by-phases. These intergrowths were not reported and discussed in a previous publication concerning the $La_2Ni_{0.9}Fe_{0.1}O_{4+\delta}$ system [51]. It may be difficult, but not impossible as shown by Kiselev et.al. [50] , to detect these phases by XRD. However, they can be seen directly in the electron microscope as seen in Figs.10 and 12.

4. Conclusions

The $La_2NiO_{4+\delta}$ system exhibits good stability in CO_2-containing atmospheres and long-term operation compared to alkaline-earth-containing oxygen-transporting membranes. Doping the membranes with a variety of ions with different valences does not improve the oxygen flux, but the process can influence the surface microstructure and grain size. Furthermore, increasing grain size by annealing for longer times at high temperatures had a negative impact on the oxygen-permeation flux. Smaller grains

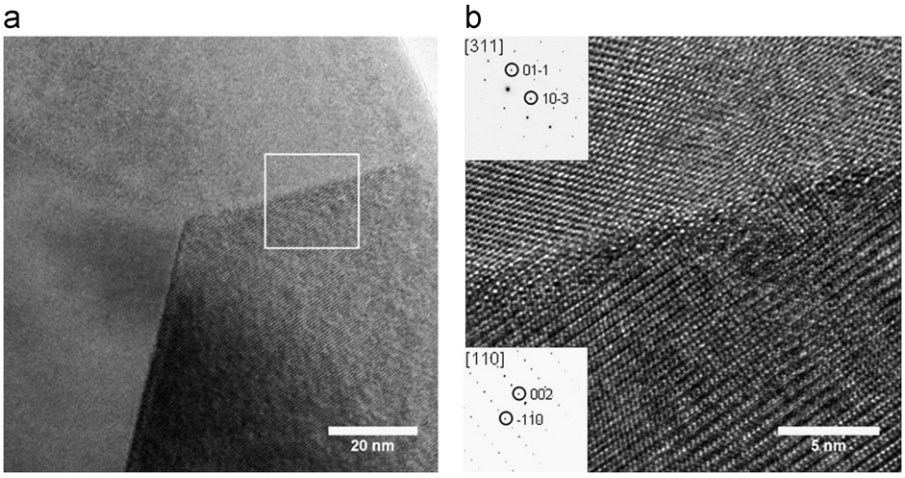

Fig. 11. (a) Bright-field TEM of three grains in close contact and (b) HRTEM of the two oriented grains with insets showing the SAED patterns of the grains.

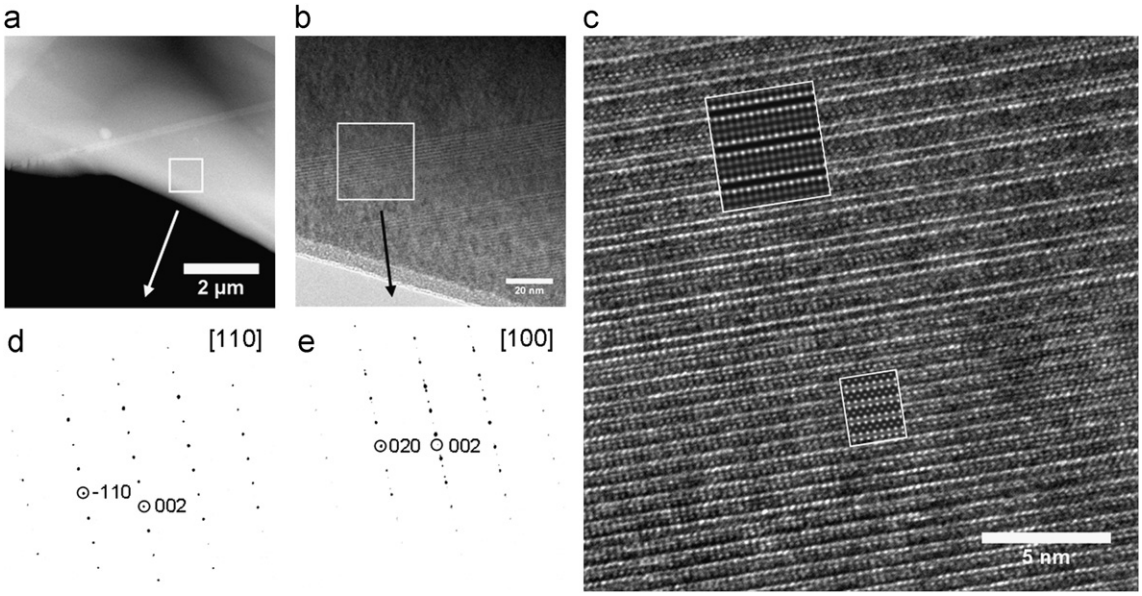

Fig. 12. (a) High-angular dark-field STEM of a $La_2Ni_{0.9}Fe_{0.1}O_{4+\delta}$ grain with lamella (b) HRTEM of a $La_2Ni_{0.9}Fe_{0.1}O_{4+\delta}$ grain with lamella (c) HRTEM of the interface between the $La_2Ni_{0.9}Fe_{0.1}O_{4+\delta}$ grain and lamella; the inset shows the image calculated with a 64 nm defocus and a sample thickness of 3.8 nm (d) SAED pattern of a $La_2Ni_{0.9}Fe_{0.1}O_{4+\delta}$ grain (e) SAED pattern of the lamella and the $La_2Ni_{0.9}Fe_{0.1}O_{4+\delta}$ host (ϕ SAED aperture 125 nm).

are beneficial for oxygen-permeation performance in the case of $La_2NiO_{4+\delta}$ and $La_2Ni_{0.9}Fe_{0.1}O_{4+\delta}$. TEM and Mössbauer experiments reveal that $La_2Ni_{0.95}Fe_{0.05}O_{4+\delta}$ is accompanied by $La_4Ni_{2.1}Fe_{0.9}O_{10-\delta}$ and La_2O_3 by-phases.

Acknowledgments

Financial support from the State of Lower Saxony in the frame of NTH bottom-up project No. 21-71023-25-7/09 is gratefully acknowledged. The authors thank Dr. M. Rodewald and Dr. J. Heindl, JEOL (Germany) GmbH, for SEM measurements.

References

[1] H. Wang, S. Werth, T. Schiestel, J. Caro, Angew. Chem. Int. Ed. 44 (2005) 6906.
[2] F.T. Akin, Y.S. Lin, J. Membr. Sci. 209 (2002) 457.
[3] C. Chen, S. Feng, S. Ran, D. Zhu, W. Liu, H.J.M. Bouwmeester, Angew. Chem. Int. Ed. 42 (2003) 5196.
[4] Z. Shao, S.M. Haile, Nature 431 (2004) 170.
[5] R. Bredesen, K. Jordal, O. Bolland, Chem. Eng. Process. 43 (2004) 1129.
[6] Y. Teraoka, H. Zhang, S. Furukawa, N. Yamazoe, Chem. Lett. 11 (1985) 1743.
[7] Z. Shao, W. Yang, Y. Cong, H. Dong, J. Tong, G.J. Xiong, J. Membr. Sci. 172 (2000) 177.
[8] M. Arnold, H. Wang, A. Feldhoff, J. Membr. Sci. 293 (2007) 44.
[9] J. Martynczuk, K. Efimov, L. Robben, A. Feldhoff, J. Membr. Sci. 344 (2009) 62.
[10] I. Barin, F. Sauert, G. Patzki, Thermochemical data of pure substances, third ed., vols. I and II, VCH, Weinheim, 1995.
[11] A.N. Shirsat, M. Ali, K.N.G. Kaimal, S.R. Bharadwaj, D. Das, Thermochim. Acta 399 (2003) 167.
[12] Y. Watanabe, S. Miyazaki, T. Maruyama, Y. Saito, J. Mater. Sci. Lett. 5 (1996) 135.
[13] K. Efimov, M. Arnold, J. Martynczuk, A. Feldhoff, J. Am. Ceram. Soc. 92 (2008) 876.
[14] K. Eichhorn Colombo, V.V. Kharton, A.P. Viskup, A.V. Kovalevsky, A.L. Shaula, O. Bolland, J. Solid State Electrochem. 15 (2011) 329.
[15] S. McIntosh, J.F. Vente, W.G. Haije, D.H.A. Blank, H.J.M. Bouwmeester, Chem. Mater. 18 (2006) 2187.
[16] J.F. Vente, W.G. Haije, Z.S. Rak, J. Membr. Sci 177 (2006) 2245.
[17] M. Al Daroukh, V.V. Vashook, H. Ullmann, F. Tietz, I. Arual Raj, Solid State Ionics 158 (2003) 141.
[18] G. Amow, S.J. Skinner, J. Solid State Electrochem. 10 (2006) 538.
[19] L. Minervini, R.W. Grimes, J.A. Kilner, K.E. Sickafus, J. Mater. Chem. 10 (2000) 2349.
[20] Z. Hiroi, T. Obata, M. Takano, Y. Bando, Phys. Rev. B 41 (1990) 11665.
[21] A. Demourgues, F. Weill, B. Darriet, A. Wattiaux, J.C. Grenier, P. Gravereau, M. Pouchard, J. Solid State Chem. 106 (1993) 317.

[22] S.J. Skinner, Solid State Sci. 5 (2003) 419.
[23] J. Martynczuk, M. Arnold, A. Feldhoff, J. Membr. Sci. 322 (2008) 375.
[24] L. Tan, X. Gu, L. Yang, W. Jin, L. Zhang, N. Xu, J. Membr. Sci. 212 (2003) 157.
[25] A.L. Shaula, R.O. Fuentes, F.M. Figueiredo, V.V. Kharton, F.M.B. Marques, J.R. Frade, J. Eur. Ceram. Soc. 25 (2005) 2613.
[26] K. Zhang, Y.L. Yang, D. Ponnusamy, A.J. Jacobson, K. Salama, J. Mater. Sci. 34 (1999) 1367.
[27] J. Martynczuk, M. Arnold, J. Caro, H. Wang, A. Feldhoff, Adv. Mater. 19 (2007) 2134.
[28] A. Feldhoff, M. Arnold, J. Martynczuk, T.M. Gesing, H. Wang, Solid State Sci. 10 (2008) 689.
[29] A. Feldhoff, J. Martynczuk, H. Wang, Prog. Solid State Chem. 35 (2007) 339.
[30] K. Lagarec, D.G. Rancourt, Nucl. Instrum. Methods Phys. Res. Sect. B 129 (1972) 266.
[31] H. Wang, C. Tablet, A. Feldhoff, J. Caro, J. Membr. Sci. 262 (2005) 20.
[32] D.E. Rice, D.J. Buttrey, J. Solid State Chem. 105 (1993) 197.
[33] B. Grande, H. Müller-Buschbaum, Z. Anorg. Allg. Chem. 433 (1977) 152.
[34] A.A. Yaremchenko, V.V. Kharton, M.V. Patrakeev, J.R. Frade, J. Mater. Chem. 13 (2003) 1136.
[35] V.V. Kharton, A.P. Viskup, E.N. Naumovich, F.M.B. Marques, J. Mater. Chem. 9 (1999) 2623.
[36] K. Efimov, T. Halfer, A. Kuhn, P. Heitjans, J. Caro, A. Feldhoff, Chem. Mater. 22 (2010) 1540.
[37] A. Feldhoff, J. Martynczuk, M. Arnold, M. Myndyk, I. Bergmann, V. Šepelák, W. Gruner, U. Vogt, A. Hähnel, J. Woltersdorf, J. Solid State Chem. 182 (2009) 2961.
[38] M.D. Abramoff, P.J. Magelhaes, S.J. Ram, Biophotonics Int. 11 (2004) 36.
[39] E.N. Naumovich, V.V. Kharton, J. Mol. Struct. 946 (2010) 57.
[40] V.V. Kharton, E.V. Tsipis, E.N. Naumovich, A. Thursfield, M.V. Patrakeev, V.A. Kolotygin, J.C. Waerenborg, I.S. Metcalfe, J. Solid State Chem. 181 (2008) 1425.
[41] R. Sayers, R.A. De Souza, J.A. Kilner, S.J. Skinner, Solid State Ionics 181 (2010) 386.
[42] E.V. Tsipis, E.N. Naumovich, A.L. Shaula, M.V. Patrakeev, J.C. Waerenborgh, V.V. Kharton, Solid State Ionics 179 (2008) 57.
[43] J.E. ten Elshof, H.J.M. Bouwmeester, H. Verweij, Solid State Ionics 89 (1996) 81.
[44] J.A. Lane, J.A. Kilner, Solid State Ionics 136–137 (2000) 927.
[45] K. Yashiro, S. Onuma, A. Kaimai, Y. Nigara, T. Kawada, J. Mizusaki, K. Kawamura, T. Horita, H. Yokokawa, Solid State Ionics 152–153 (2002) 469.
[46] I.V. Khromushin, T.I. Aksenova, Zh.R. Zhotabaev, Solid State Ionics 162 (2003) 37.
[47] F. Menil, J. Phys. Chem. Solids 46 (1985) 763.
[48] K.L. da Silva, A. Börger, K.-D. Becker, F. Tietz, D. Stöver, Solid State Ionics 192 (2011) 552.
[49] J. Fontcuberta, G. Longworth, J.B. Goodenough, Phys. Rev. B 30 (11) (1984) 6320.
[50] E.A. Kiselev, N.V. Proskurnina, V.I. Voronin, V.A. Cherepanov, Inorg. Mater. 43 (5) (2007) 167.
[51] E.V. Tsipis, E.N. Naumovich, M.V. Patrakeev, J.C. Waerenborgh, Y.V. Pivak, B. Gaczynski, V.V. Kharton, J. Phys. Chem. Solids 68 (2007) 1443.
[52] E.V. Tsipis, M.V. Patrakeev, J.C. Waerenborgh, Y.V. Pivak, A.A. Markov, P. Gaczynski, E.N. Naumovich, V.V. Kharton, J. Solid State Chem. (2007) 1902.